CERN - European Organization for Nuclear Research

LCD-Note-2011-026

Top Quark Pair Production at a 500 GeV CLIC Collider

Katja Seidel[*†], Stephane Poss[‡] and Frank Simon[*†]

[*] *Max-Planck-Institut für Physik, Munich, Germany,*
[†] *Excellence Cluster 'Universe', TU München, Garching, Germany,*
[‡] *CERN, Geneva, Switzerland*

April 7, 2012

Abstract

We present a study of the capability of a 500 GeV e^+e^- collider based on the CLIC technology for precision measurements of top quark properties. The analysis is based on full detector simulations of the CLIC_ILD detector concept using Geant4, including realistic beam-induced background contributions from two photon processes. Event reconstruction is performed using a particle flow algorithm with stringent cuts to control the influence of background. The mass and width of the top quark are studied in fully-hadronic and semi-leptonic decays of $t\bar{t}$ pairs using event samples of signal and standard model background processes corresponding to an integrated luminosity of 100 fb^{-1}. Statistical uncertainties of the top mass of 0.08 GeV and 0.09 GeV were obtained for the fully-hadronic channel and the semi-leptonic channel, respectively. The results are compared to a similar analysis performed within the framework of the ILC, showing that a similar precision can be achieved at CLIC despite less favorable experimental conditions.

Contents

1. Introduction

The top quark plays a unique role in particle physics. Due to its high mass, it is particularly sensitive to new physics and is intimately connected to the mechanism of electroweak symmetry breaking. It has sizable impact on the Higgs boson mass through radiative corrections, and, together with the W boson mass, drives electroweak predictions for the Higgs mass. Due to its short lifetime, the top quark decays before hadronizing, offering the unique opportunity to study a bare quark by accessing its properties directly through its decay products. Top quarks decay electroweakly, into a real W boson and a down-type quark. Due to the large bt CKM matrix element, the decay is almost exclusively into a W boson and a b quark.

To date, top quarks have been observed at the Tevatron and at the LHC. At present, the best measurement of the mass is provided by the Tevatron, with a statistical error of 0.6 GeV [1]. The measurement is already limited by systematics, with a total systematic error of 0.75 GeV. Early LHC analyses obtained statistical errors on the order of 1 GeV to 2 GeV, with systematic errors close to 3 GeV [2, 3]. With increasing integrated luminosity, significant improvement is anticipated, but the systematics are expected to remain substantial due to the challenging environment of hadron colliders and due to theoretical uncertainties [4].

Significant improvements are expected in e^+e^- collisions, which provide a cleaner experimental environment. The theoretically cleanest way of measuring the top quark mass is by means of a threshold scan. Studies suggest that combined theoretical and experimental errors of the order of 100 MeV can be achieved with this technique. A drawback of this technique is that a threshold scan requires the collider to be operated for a single measurement over an extended period, conflicting with other studies to be performed at such a machine. It is thus attractive to explore the possibilities for top property measurements in $t\bar{t}$ production well above threshold, reconstructing the top from its decay products, the same technique as used in hadron colliders. Here, the theoretical interpretation of the observations is more challenging, but progress has been made recently in establishing connections between the top mass parameter used in theory and the experimentally observable invariant mass of the decay products [5, 6].

The relatively clean environment of e^+e^- collisions, combined with the expected jet energy and track momentum resolution of linear collider detectors, makes precision measurements in fully-hadronic ($e^+e^- \to t\bar{t} \to q\bar{q}b\,q\bar{q}b$) and semi-leptonic ($e^+e^- \to t\bar{t} \to q\bar{q}b\,l\nu b$) decay channels, the channels with the highest branching fraction, possible. For the ILC, studies with full detector simulations have shown that statistical errors below 100 MeV can be achieved for integrated luminosities of 100 fb^{-1} at $\sqrt{s} = 500$ GeV [7].

2. Experimental Conditions at a 500 GeV CLIC Collider

The Compact Linear Collider CLIC is a collider concept based on normal conducting accelerating cavities and two-beam acceleration, which is designed to provide up to 3 TeV collision energy. In a staged approach, a shorter, lower energy version would be operated initially, while construction is under way for the full energy phase.

In the present note, we study the case of a 500 GeV CLIC machine, which is directly comparable to the baseline design of the International Linear Collider. The use of a different accelerator

technology compared to the ILC leads to differences in the experimental environment which could potentially have a negative impact on the physics performance. The most important parameter here is the time between bunch crossings within a bunch train, which is 0.5 ns in the case of CLIC, while it is 356 ns or 670 ns in the case of the ILC, depending on the adopted design. For typical detector integration times of the order of a few ns to 100 ns, the short bunch crossing time leads to the pile-up of background from many bunch crossings over the 177 ns long bunch trains. In addition, the smaller beam spot size at CLIC leads to increased beamstrahlung and correspondingly larger energy spread, with $\sim$61 % of the total luminosity within 1 % around the peak energy, compared to $\sim$72 % at the ILC. This translates into larger uncertainties when using energy or momentum constraints along the beam axis.

The radiated photons lead to background through the creation of coherent and incoherent e^+e^- pairs as well as incoherent quark pair production, which results in hadronic events. While the coherent pairs are emitted at very small angles, defining the crossing angle of the machine, the incoherent pairs have higher transverse momenta and constrain the dimension of the beam pipe in the experiment as well as the radius of the vertex detector. The hadron background affects all aspects of the event reconstruction, in particular jet energy measurements. At a 500 GeV CLIC machine, 0.3 $\gamma\gamma \rightarrow$ hadrons events per bunch crossing are expected, with an energy of 13.3 GeV. 3.4 GeV of energy are deposited in the calorimeter system, of which 0.2 GeV in the barrel detectors.

The detector model used in the present study is a variant of CLIC_ILD [8], a detector concept based on Particle Flow event reconstruction. It consists of a low-mass, high-precision vertex detector and an inner silicon tracker, surrounded by a large-volume time projection chamber, followed by highly granular electromagnetic and hadronic calorimeters contained inside a 4 T solenoidal magnet with instrumented flux return for muon identification. The detector design is based on the ILD detector concept for the ILC, adapted to account for the higher energy (3 TeV) and more severe background conditions at CLIC. This leads to an increased radius of the innermost layer of the vertex detector, which sits at 31 mm compared to 16 mm in ILD at the ILC. At 500 GeV, the background is significantly reduced compared to the 3 TeV case, permitting modifications of the detector to optimize its performance for the lower collision energy. In particular the innermost vertex detector layer for CLIC_ILD can move in by 6 mm to a radius of 25 mm, improving flavor tagging at low momentum. To distinguish the modified detector design from the 3 TeV design, the detector model is referred to as CLIC_ILD_CDR500.

Minimization of the impact of the hadronic background requires strict timing cuts on the reconstructed particles to limit the influence of out-of-time contributions. Here, timing in the calorimeters is of particular importance.

3. Event Generation, Simulation and Reconstruction

The signal process studied in this note is top quark pair production, $e^+e^- \rightarrow t\bar{t}$, which, at a 500 GeV CLIC collider, has a cross section of approximately 528 fb. The top quark decays almost exclusively into a W boson and a b quark. The signal events can thus be grouped into different classes, according to the decay of the W bosons. These are the *fully-hadronic* channel, with both Ws decaying into quark pairs, the *semi-leptonic* channel, with one W decaying into

$\sqrt{s} = 500\,\text{GeV}$

type	$e^+e^- \rightarrow$	cross section σ	number of events number of generated events
Signal (m_{top} =174 GeV)	$t\bar{t}$	528 fb	$5.3 \cdot 10^4$
Background	WW	7.1 pb	$7.1 \cdot 10^5$
Background	ZZ	410 fb	$4.1 \cdot 10^4$
Background	$q\bar{q}$	2.6 pb	$2.6 \cdot 10^5$
Background	WWZ	40 fb	$4.0 \cdot 10^3$
Signal control (m_{top} =175 GeV)	$t\bar{t}$	528 fb	$5.3 \cdot 10^4$
Signal control (m_{top} =174 GeV)	$t\bar{t}$	528 pb	$1.2 \cdot 10^5$

Table 1: Signal and considered physics background processes, with their cross section calculated for CLIC at 500 GeV. Signal and background events were generated for and integrated luminosity of 100 fb^{-1}. Only the signal control sample with a generated top mass of 174 GeV twice the number of statistics was generated and simulated.

quarks, the other into a lepton and the corresponding neutrino, and the *fully-leptonic* channel, with both Ws decaying into lepton and neutrino. In the leptonic channels, the decay into a τ and neutrino is a special case, since the τ decays almost instantly into either a lepton and two neutrinos or into one or more hadrons and a neutrino, giving rise to additional missing energy in the final state, and potential confusion with hadronic decay modes.

In the analysis, only fully-hadronic and semi-leptonic events, excluding τ final states, were selected, since those provide the best possible mass measurement. However, to account for imperfect event classification, all possible decay modes of the $t\bar{t}$ pair were generated according to their branching fractions and included in the signal sample. The top mass and width were fixed for the signal event sample to $m_{\text{top}} = 174.0\,\text{GeV}$ and $\sigma_{\text{top}} = 1.37\,\text{GeV}$.

In addition to the signal, background processes with similar event topologies have to be considered. These are mostly four and six fermion final states, with the high cross-section quark pair production in addition. Table 1 lists the studied processes, with approximate cross sections at a 500 GeV CLIC machine, and the corresponding event numbers that were generated for an integrated luminosity of 100 fb^{-1}. In addition, the processes $e^+e^- \rightarrow q\bar{q}e^+e^-$ and $e^+e^- \rightarrow q\bar{q}e\nu$, which are dominated by t-channel single boson production, were investigated using samples with reduced statistics. It was shown that the non-di-boson contributions are rejected completely in the analysis. Since the di-boson contributions are accounted for in the $e^+e^- \rightarrow WW$ and $e^+e^- \rightarrow ZZ$ modes, they were not considered in the final production of 100 fb^{-1}. In addition to the signal and background processes two control signal events samples were generated in addition. One with a different generated top mass and top width (m_{top} =175 GeV, σ_{top} =1.5 GeV), to study possible effect in the the final fit (Subsection 4.7 and Appendix A.7). The other control sample was generated with approximately twice the statistics and was used as a signal only sample in the final fit (see Subsection 4.7).

Since WHIZARD 1.95 [9], which was used as the default event generator for the CLIC Conceptual Design Report (CDR) benchmark studies, is not correctly producing final-states and explicitly defined intermediate states with non-zero width of the particles, PYTHIA [10] was used

to generate the signal process $e^+e^- \to t\bar{t}$ as well as the two background processes $e^+e^- \to WW$ and $e^+e^- \to ZZ$. The processes with explicitly given final states, without specifying intermediate particles, $e^+e^- \to q\bar{q}$, $e^+e^- \to q\bar{q}e^+e^-$ and $e^+e^- \to q\bar{q}e\nu$ were generated with WHIZARD 1.95. Since the process $e^+e^- \to WWZ$ is not implemented in PYTHIA, WHIZARD was used for its generation. For simplicity, these events were generated with zero width for the intermediate bosons, allowing to specify defined intermediate states in WHIZARD.

The luminosity spectrum of the 500 GeV CLIC accelerator was included in the event generation for a realistic machine implementation. More information concerning the beam induced backgrounds can be found in [11, 12]. For the simulation with Mokka [13] the detector model CLIC_ILD_CDR500, briefly introduced in Section 2, was used. 300 bunch crossings of $\gamma\gamma \to$ hadrons events were overlaid with the signal event at the digitization stage. The number of overlaid bunch crossings was higher than in the 3 TeV case since at 500 GeV more relaxed timing cuts are necessary due to the increased importance of low momentum tracks for the overall jet and event energy reconstruction. The correspondingly longer integration times of the detectors required the simulation of the background accumulated over a more extensive period. The tracking and particle flow event reconstruction was then performed on the combined event comprising signal and beam-induced background.

The background from $\gamma\gamma \to$ hadrons processes is one of the major challenges at CLIC due to the high collision frequency of 2 GHz. Mitigation of the influence of this background requires precise time stamping to assign energy deposits to individual bunch crossings, and cuts based on the transverse momentum of particles, since the background particles are predominantly at low p_T in the forward and backward region of the detector. Different sets of cuts with varying severity in timing and p_T were applied to the reconstructed particles (Particle Flow Objects - PFOs) and stored for further analysis. These sets were labeled *no cut*, *loose*, *default* and *tight*.

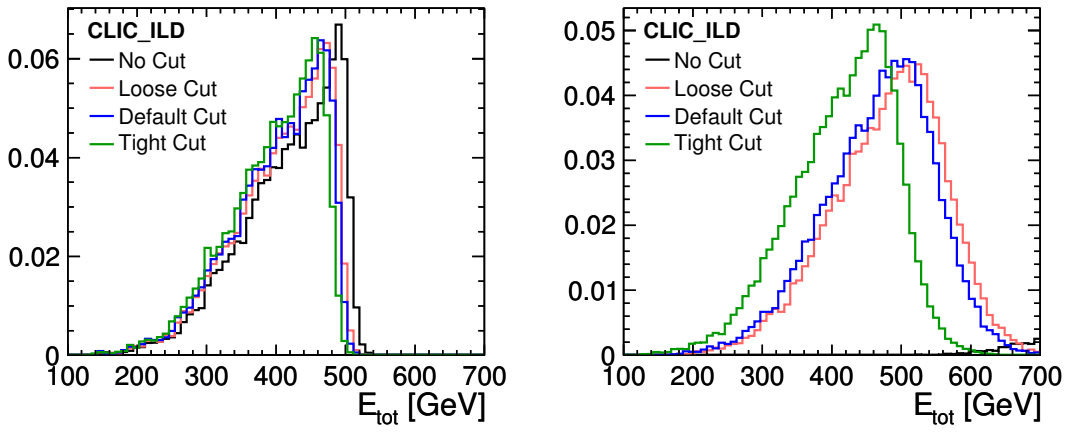

Figure 1: Effect of timing and p_t cuts for events without (*left*) and with overlaid $\gamma\gamma \to$ hadron events (*right*).

Figure 1 shows the effect of these four sets of PFO selections on the total visible energy in

$e^+e^- \to t\bar{t}$ signal events, both for the case without and with overlaid $\gamma\gamma \to$ hadrons background. While too loose cuts result in significant pick-up of additional energy, too tight cuts lead to a loss of signal particles. Significant loss of signal energy leads to a deterioration of mass resolution due to missing information, while excessive background reduces flavor tagging efficiency, in addition to negative effects on the mass resolution. Following detailed studies of the different cut sets, the *default* cut option (cuts are stated in Appendix A.1), implemented in the *SelectedPandoraPFANewPFOCollection*, was chosen.

4. Data Analysis

The data analysis proceeds in several steps, described in the following. In general, the present analysis scheme is similar to the $t\bar{t}$ analysis performed for the ILD Letter of Intent. Due to a more general input sample including semi-leptonic τ events as well as fully-leptonic events, and due to the different bunch and beam structure of the CLIC machine, some steps had to be introduced in addition and major strategy changes had to be adopted for other steps. In general, the analysis was optimized to provide precise measurements of the top quark mass and width, favoring strict rejection of imperfectly reconstructed events over the maximization of reconstructed top quark candidates.

As a first step, the *Lepton Finder*, see Section 4.1, was used to classify all events as fully-hadronic (no isolated lepton found), semi-leptonic (exactly one isolated lepton found) or fully-leptonic (at least two isolated leptons found), according to the number of isolated leptons found. Events classified as fully-leptonic were rejected, while the other two classes were clustered into four or six jets, according to event class, as described in Section 4.2. Following this, a *Flavor Tagging* algorithm was used to identify the two jets originating from b quarks, as described in Section 4.3. For the fully-hadronic channel the correct combination of the four non-b jets into W bosons had to be found among the three possible combinations, see Section 4.4. In the semi-leptonic case, this step was unnecessary, since the assignment of light jets and leptons to W candidates is unique. The pairing of W candidates and b jets into the two top candidates was done using a *Kinematic Fit*, exploiting constraints on the event topology to improve the top mass measurement, as discussed in Section 4.5. After *Background Rejection* using a binned likelihood technique, described in Section 4.6, the final top mass distribution was fitted to extract the top mass and width as discussed in Section 4.7.

4.1. Lepton Finder

The classification into fully-hadronic, semi-leptonic and fully-leptonic events was based on the identification of isolated leptons using a lepton finder as a first step of the analysis. It was optimized to identify charged leptons ($e^\pm$ or $\mu^\pm$) from the W decay. Since these leptons are typically highly energetic, and in contrast to leptons originating from hadronic decays in quark jets, well separated from other activity in the event, isolation and energy were used as selection criteria. A minimum lepton energy of 10 GeV was required, and for the isolation a cone around the lepton momentum axis with an opening angle of 10° was considered. The lepton candidate was classified as isolated if no other charged particle with an energy larger than 2.5 GeV was

	no $\gamma\gamma \to$ hadron events overlaid	$\gamma\gamma \to$ hadron events overlaid
Semi-leptonic events correctly identified (single isolated lepton found)	93 %	91 %
All-hadronic events correctly identified (no isolated lepton found)	97 %	96 %
All-leptonic events correctly identified (more than one isolated leptons found)	57 %	57 %

Table 2: Selection efficiency of the lepton finder for the various $t\bar{t}$ event classes, with and without the inclusion of overlaid background events.

measured inside the cone. The energy cut values and the cone opening angle were determined with a parameter scan using the true Monte Carlo information of a $t\bar{t}$ event sample. All events in which more than one isolated lepton was found were classified as fully-leptonic and were consequently rejected for the further analysis.

The efficiency for semi-leptonic and fully-hadronic events to be classified correctly by the lepton finder is summarized in Table 2 for events with and without $\gamma\gamma \to$ hadron events overlaid. The low selection efficiency for fully-leptonic events is due to the fact that here events with one or two τ leptons in the final state are included in the sample. For those events, the rejection is considerably less efficient due to the large branching fraction of hadronic τ decays and due to the reduced momentum of leptons from leptonic τ decays.

4.2. Jet Clustering

Jet clustering of the events was performed according to the classification of the lepton finder. At this stage the event sample was split into a fully-hadronic and a semi-leptonic branch. In the fully-hadronic branch, events were forced to be clustered in 6 jets, while for the semi-leptonic branch 4 jets were required. In the latter, the isolated lepton was excluded from jet finding.

In the $t\bar{t}$ analysis performed for the ILC LoIs, the Durham jet algorithm was used. This was not possible under the CLIC beam background conditions since too many background particles in the forward region are picked up to be included in the jets due to the distance measure of the Durham algorithm, which is given by the angular distance between particles. Instead, the k_t algorithm with a $\Delta\eta, \Delta\phi$ metric from the FastJet package [14] was used. In this case, the particle distance is increased in the forward region, leading to the inclusion of more background particles in the not-considered beam jets, making the jet clustering more robust against $\gamma\gamma \to$ hadrons events. Jet finding was performed in exclusive mode, meaning that an event was clustered into a fixed number of jets. The k_t jet algorithm was used with a jet size parameter R of 1.3, which was selected as the best trade-off between the requirements to not loose signal particles and to limit the inclusion of background. This is illustrated in Figure 2, which shows the total reconstructed energy in jets and isolated leptons as a function of the jet size parameter, both for events with and without $\gamma\gamma \to$ hadrons background and for a variety of jet size parameters. For R below 1.3, significant signal energy loss is apparent, while the largest jet sizes result in a broadening of the

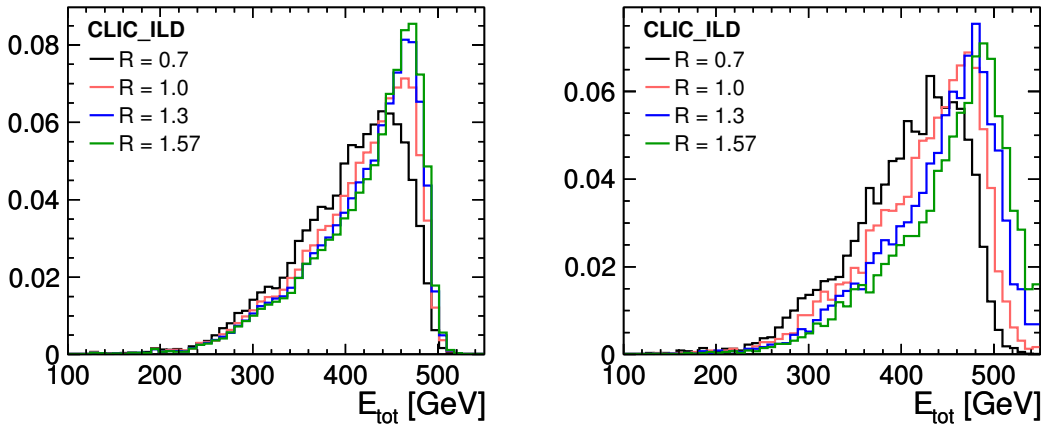

Figure 2: Efffect of the size of the R parameter in the k_t jet-algorithm for the signal samples without (*left*) and with overlaid $\gamma\gamma \rightarrow$ hadron events (*right*).

total energy distribution due to background pick-up.

In the following discussions we will refer to the different analysis branches (semi-leptonic event candidates and fully-hadronic event candidates) as the *4 jet sample* and the *6 jet sample* for convenience.

4.3. Flavor Tagging

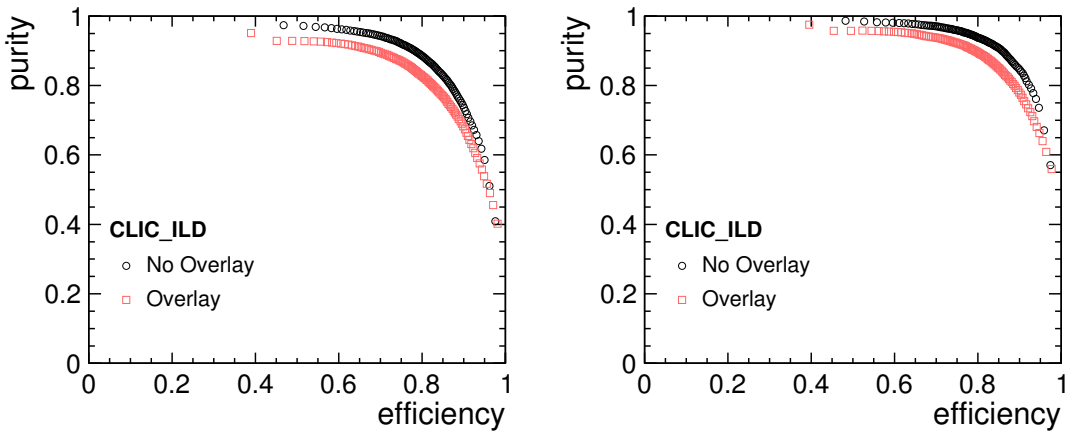

Figure 3: Efficiency versus purity of *b*-tagging for the signal sample with and without overlaid $\gamma\gamma \rightarrow$ hadron events in the full-hadronic decay channel (*left*) and the semi-leptonic decay channel (*right*).

Efficient b-tagging is essential for the identification of $t\bar{t} \to (bq\bar{q})(\bar{b}q\bar{q})$ and $t\bar{t} \to (bq\bar{q})(\bar{b}l\nu_l)$ events compared to multi-fermion background, and is also crucial for the correct assignment of jets to top candidates for signal events. Flavor tagging was performed using the *LCFI Flavour Tagging* [15] package. This algorithm uses input variables for a neural network, which provides b and c jet probabilities ("b-tag") for each jet in the event, depending on a number of input variables. The input values for the neural network are shown in Fig. 13 of Appendix A.2 for the 6 and 4 jet signal samples.
Neural network training was performed using a 6 jet sample of $t\bar{t}$ events. These events were generated and reconstructed without beam spectrum, initial state radiation and top width, but did contain all other generation, simulation and reconstruction detail, such as overlaid $\gamma\gamma \to$ hadrons events.

The b-tagging efficiency versus purity for the signal event sample used in this analysis is shown in Figure 3 for 6 jets (left) and 4 jets (right).

4.4. Jet combinatorics

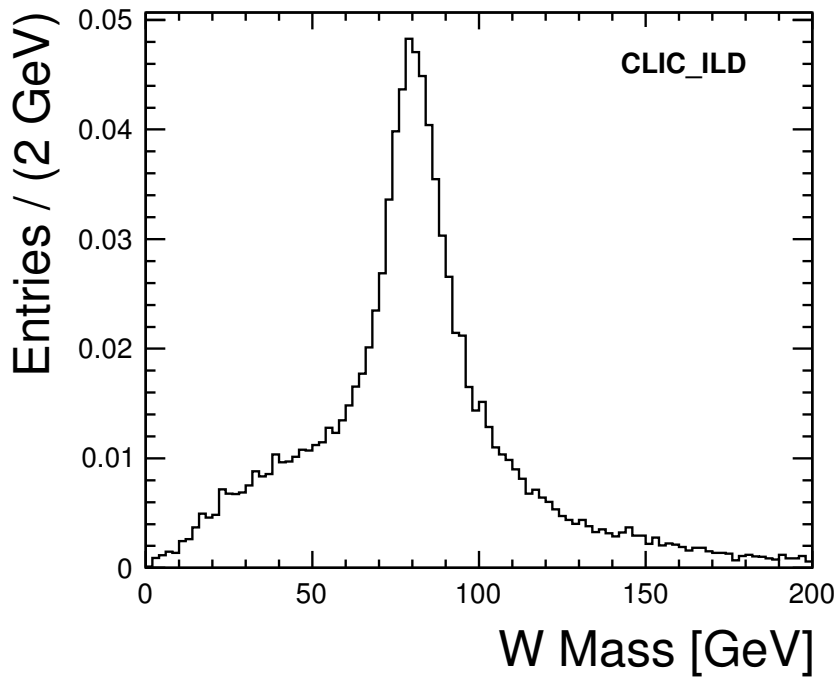

Figure 4: W reconstruction in the semi-leptonic channel. One W is reconstructed from the four-momentum of the two light-jets in the 4 jet sample. The other W boson is reconstructed from the measured lepton and missing energy. The momentum of the missing energy is given by the negative sum of all other measured objects.

For both samples, the two jets with the highest b-tag values were classified as jets created by

a b quark (b jets). All other jets were classified as light-jets (created by u, d, s or c quarks), originating from the W boson decay.

In case of the 4 jet sample all decay products of the $t\bar{t}$ pair are found at this stage of the analysis: 2 b jets, 2 light-jets forming one W boson, one charged lepton and a neutrino forming the other W boson. Since the neutrino is unmeasured, its momentum is taken to be the total missing momentum. The resulting mass distribution of the two W bosons is shown in Figure 4. Since the neutrino absorbs all energy reconstruction uncertainties, and since the missing energy measurement also includes contributions from the beam energy spectrum, the leptonic W boson mass is significantly less well constrained than the hadronic W boson mass. This is apparent from the comparison of the semi-leptonic distribution with the distribution measured in the fully-hadronic case, discussed in the following.

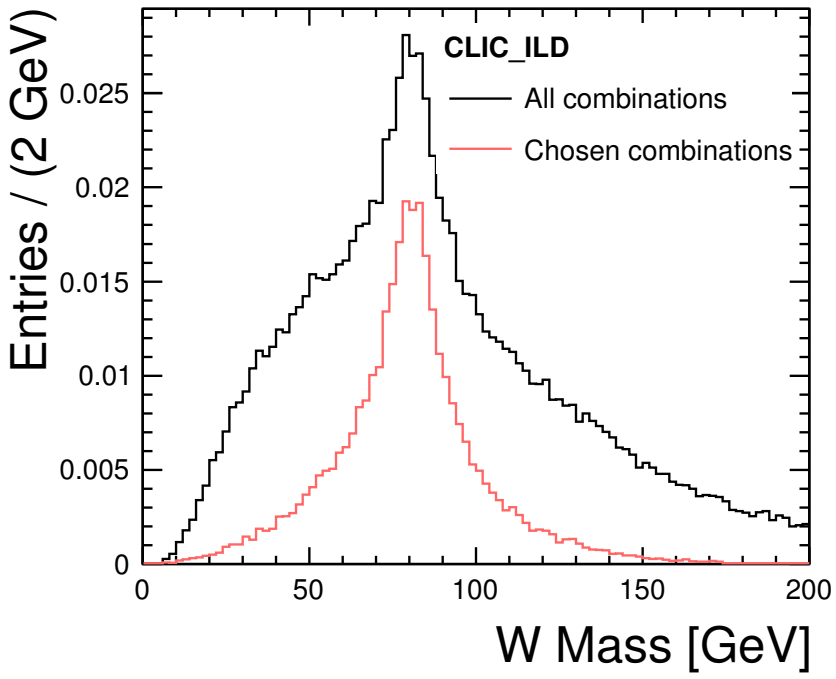

Figure 5: Effect of jet combinatorics for the W bososn reconstruction in the 6 jet channel. Black: All possible jet-pair combinations from the set of four light-jets. Red: Chosen jet combinations. The number of chosen combinations is reduced by a factor of three compared to all combinations due to the three possible pairings for the four light jets.

In the 6 jet case, the correct pairing of light-jets into W bosons has to be identified among the three possible permutations of light-jet pairs. For each permutation the invariant mass of both jet pairs was calculated and compared with the true W boson mass. The permutation with the minimal value of

$$v = |m_{ij} - m_W| + |m_{kl} - m_W|,$$

where $m_W = 80.4\,\text{GeV}$ and m_{ij} and m_{kl} are the invariant masses of two distinct jet pairs, was chosen as the correct combination. Figure 5 shows the invariant mass of all possible light-jet pair combinations, and the chosen combinations to form W boson candidates.

After this step all decay products of the $t\bar{t}$ pair in the full-hadronic channel are uniquely assigned.

4.5. Kinematic Fit

After the identification of b jets and the pairing of light jets and leptons into W bosons, the next step of the analysis is the correct grouping of W boson candidates and b jets into top quarks. This assignment was performed using a kinematic fit. Out of the two possible combinations, the one with the higher probability of the kinematic fit result was chosen as the correct combination of W bosons and b jets into top candidates.

A kinematic fit, implemented in this analysis using the MarlinKinFit package [16], uses kinematic constraints on the given physical process, in this case the $t\bar{t}$ decay, to improve the precision of the event parameters of interest.

The parameters of interest are calculated / fitted using a least squares technique and the physical constraints are incorporated into the fit using Lagrange multipliers. Constraints can be hard or soft constraints. Hard constraints have to be fulfilled by the fitter. For soft constraints on a parameter the fitter has to fulfill the constraints in a certain range with a given functional form provided to the fitter as input. Here, only hard constraints are used since those have shown the best performance. This creates some issues in combination with the beam energy spectrum, which results in a sizable fraction of events with non-zero momentum along the beam axis and with reduced center of mass energy, as discussed below.

The following constraints were used in the kinematic fit:

- energy conservation $\sum_i E_i = 500\,\text{GeV}$
- momentum conservation
  - $\sum_i p_{x,i} = 5\,\text{GeV}$, due to the beam crossing angle of 20 mrad
  - $\sum_i p_{y,i} = 0\,\text{GeV}$
  - $\sum_i p_{z,i} = 0\,\text{GeV}$
- correct W boson mass measurements
  - $|m_{W_1} - m_W| = 0\,\text{GeV}$
  - $|m_{W_2} - m_W| = 0\,\text{GeV}$
- equal mass of both top candidates $|m_{t_1} - m_{t_2}| = 0\,\text{GeV}$

with a nominal W boson mass of m_W =80.4 GeV.

The input to the kinematic fit in case of the 6 jet sample are the four-momenta of the light jets, already paired into W bosons and the four-momenta of the b jets. In case of the 4 jet sample the input are the four-momenta of the light jets and b jets as well as of the isolated lepton. In the

latter case, also the unmeasured neutrino is represented in the fit, with starting values set to the measured missing energy and momentum in the event.

During the fit procedure, the fitter varies the particle momenta and energies to fulfill the constraints. This is done according to the detector resolution for the various input particles, both in energy and azimuthal and polar angle. The angular resolutions for jets and angular and energy resolutions for leptons were derived from Monte Carlo studies of the $t\bar{t}$ sample (see Appendix A.3) and are parametrized as

$$\begin{aligned} \text{Jets} \quad &: \quad \sigma_E = 4.5\% \cdot E_{jet} \quad \sigma_\theta = 0.27\,\text{rad} \cdot \text{GeV}/\sqrt{E_{jet}} \quad \sigma_\phi = 0.25\,\text{rad} \cdot \text{GeV}/\sqrt{E_{jet}} \\ \text{Leptons} \quad &: \quad \sigma_p = 1.5 \cdot 10^{-4} \cdot E_l^2 \quad \sigma_\theta = 5\,\text{mrad} \quad \sigma_\phi = 15\,\text{mrad}. \end{aligned}$$

The uncertainty of the energy resolution for jets is not obtained from the signal sample, because this includes uncertainties of the quality of the jet clustering, and thus correlations between the jets belonging to one original parent particle, resulting in an overestimation of the energy uncertainties. Since these correlations are not taken into account in the kinematic fit, the uncertainties expected for single jets [17] are used as input parameters.

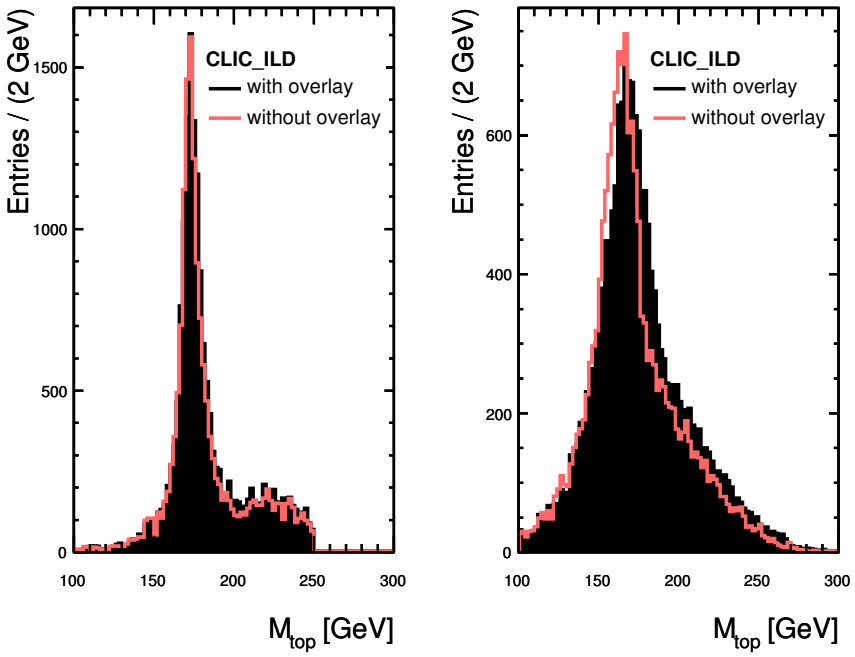

Figure 6: Reconstructed top mass distribution for the 6 jet channel without (right) and with (left) kinematic fit. The black lines show the top mass distribution for events with overlaid $\gamma\gamma \to$ hadrons events, the red lines show events without. The high-mass bump in the mass distribution obtained with kinematic fit is due to kinematic reflections for events with incorrect assignment of jets to top candidates.

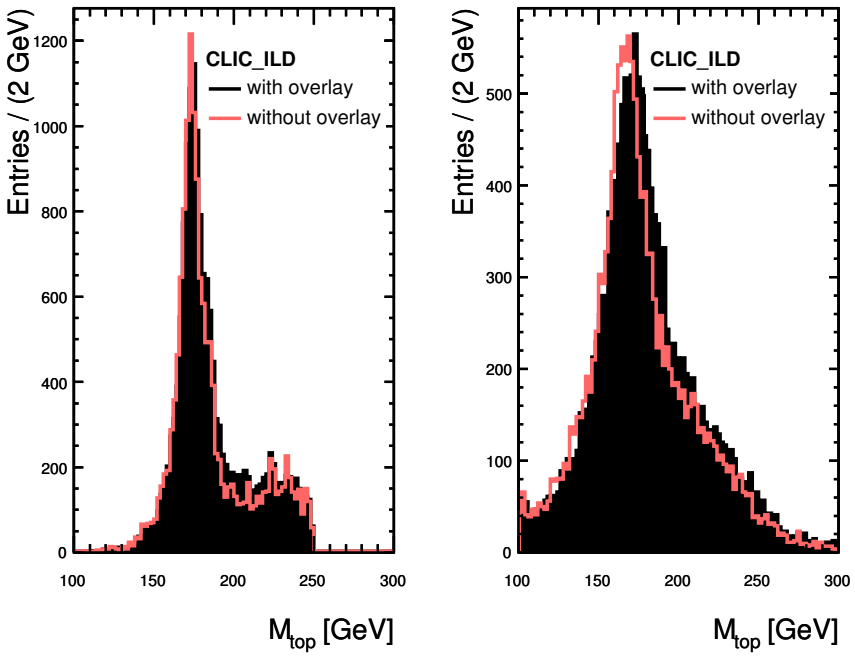

Figure 7: Reconstructed top mass distribution for the 4 jet channel without (right) and with (left) kinematic fit. The black lines show the top mass distribution for events with overlaid $\gamma\gamma \to$ hadrons events, the red lines show events without. The high-mass bump in the mass distribution obtained with kinematic fit is due to kinematic reflections for events with incorrect assignment of jets and/or leptons to top candidates.

The fit fails if it is unable to satisfy the constraints outlined above within the allowed modifications of the input parameters. It is observed that some of the fit failures are due to the wrong identification of one of the b jets. This is particularly likely in the case of a W decaying into a charm quark and another light quark. Thus, to improve the number of successful fits and to account for possible wrong flavor tagging the kinematic fit is repeated for unsuccessful kinematic fits after exchanging the b jet with the lower b-tag value and the light-jet with the highest b-tag value. This procedure increases the number of successful kinematic fits by $\sim 20\,\%$.

The result of the kinematic fit, compared to the top mass reconstruction without kinematic fit, is shown in Figure 6 for the 6 jet case and in Figure 7 for the 4 jet case.

Both the 4 and 6 jet samples contain semi-leptonic events with τ decays and fully-leptonic events (with and without τ decays). The majority of events from τ decays of semi-leptonic or fully-leptonic events were grouped into the 6 jet sample due to the dominating hadronic decay of the τ lepton. Due to the additional neutrino in the final state and the corresponding additional missing energy and momentum, 99 % (93 %) of the τ events fail the kinematic fit for the 6 jet (4 jet) event sample, eliminating the problematic τ events from the final sample. From the

	Background rejection efficiency [%]	
$e^+e^- \rightarrow$	6-jet events	4 jet events
$q\bar{q}$	97.0	97.3
WW	94.6	85.7
ZZ	94.1	94.0
WWZ	13.1	25.2

Table 3: Background rejection efficiency of kinematic fit.

remaining τ events in the final 6 jet (4 jet) sample 0 % (39 %) are τ decays from fully-leptonic events.

The isolated lepton finder (see Section 4.1) rejected approximately 56 % of the fully-leptonic events. The remaining fraction is mainly contained in the 4 jet sample, of which 95 % are rejected by the kinematic fit. Finally the fraction of semi-leptonic events with τ decays and fully-leptonic events in the final sample is 1.3 % (2.7 %) for the 6 jet (4 jet) sample.

The overall rate of successful fits for true signal events (without τ events) in the 6 jet (fully-hadronic top pair decays) and the 4 jet (semi-leptonic top pair decays) was $\sim$37% and $\sim$60%, respectively. The relatively large failure rate of the kinematic fit is due to imperfectly reconstructed fit objects. Several effects are expected to contribute to this: wrong classification into the semi-leptonic and fully-hadronic event branch, imperfect jet clustering, W boson reconstruction from the wrong jet combination, too large remaining $\gamma\gamma \rightarrow$ hadrons background or large effects of beamstrahlung. The correlation of fit success with the quality of the W boson reconstruction and the influence of the beam energy spectrum is discussed further in Appendix A.4. The relatively low success rate of the kinematic fit reflects the orientation of the analysis towards precision measurements of the top quark mass, which is best performed in optimally reconstructed events.

Since the kinematic fit places stringent constraints on the overall event topology, it also serves as a powerful rejection of non-$t\bar{t}$ background. A large fraction of events from the considered background samples fail the fit, as summarized in Table 3.

4.6. Background Rejection

In addition to the rejection of physics background by the kinematic fit, further signal and background discrimination was needed to further purify the signal. This was achieved by means of a binned likelihood technique [18] which combines several discrimination variables into one likelihood variable. For the two event classes j, "signal" and "background", probability density functions $f^j(x_i)$ for each discriminating variable x_i were provided as input to the likelihood algorithm. The probability $p^j(x_i)$ for a given event to belong to event class j for a given value of the discriminating variable x_i is given by

$$p^j(x_i) = \frac{f^j(x_i)}{\sum_k f^k(x_i)},$$

where k runs over all event classes.

The final likelihood for an event belonging to the signal event class S, combining the probabilities of the individual discrimination variables, is given by

$$L_S = \frac{\prod_i p^S(x_i)}{\sum_k \prod_i p^k(x_i)},$$

with i running over all discrimination variables and k over all event classes.

The chosen discrimination variables, shown in Figure 8, are:

- Highest b-tag
- Second highest b-tag
- Number of particles in event
- Mass of W_1 and W_2
- Difference of top masses without kinematic fit
- Sphericity
- Log (d_{cut}), which is a variable provided by the jet clustering algorithm. The d_{cut} value used in this analysis, determines for each event the maximal particle distance for which n jets are found compared to $n-1$ jets, which would result in larger values of d_{cut}. Thus, this variable is a measure of how likely it is to cluster a given event into the fixed number of n jets.

At the time of the finalization of the analysis of this note, the fully simulated event samples were not sufficient to provide two independent data sets for the determination of the probability density functions for the likelihood calculation and for the final analysis. To avoid a bias from using signal and background events both for the determination of the PDFs and in the analysis, only events with an unsuccessful kinematic fit were used in the PDF determination, resulting in statistical independence of training and analysis samples. Since the events with unsuccessful fits have somewhat different (less signal-like) characteristics than the ones passing the fit, this procedure is expected to result in a slightly decreased background rejection efficiency. To quantify this, the analysis was repeated by using all events (with and without successful kinematic fit) for the PDF determination. A decrease in background rejection efficiency of less than 0.5 % was observed for the case of statistically independent PDF determination from events failing the kinematic fit, comparing to the use of all available events. This demonstrates that the approach taken in the analysis is viable, and does not lead to a significant degradation of the results.

The signal likelihood L_S for $t\bar{t}$ and background events passing the kinematic fit are shown in Figure 9 for 4 jet and 6 jets events.

A cut on the signal likelihood L_S of 0.6 was chosen to reject background from signal events in the the 6-jet and the 4 jet sample. The resulting efficiencies for signal extraction and background rejection are summarized in Table 4.

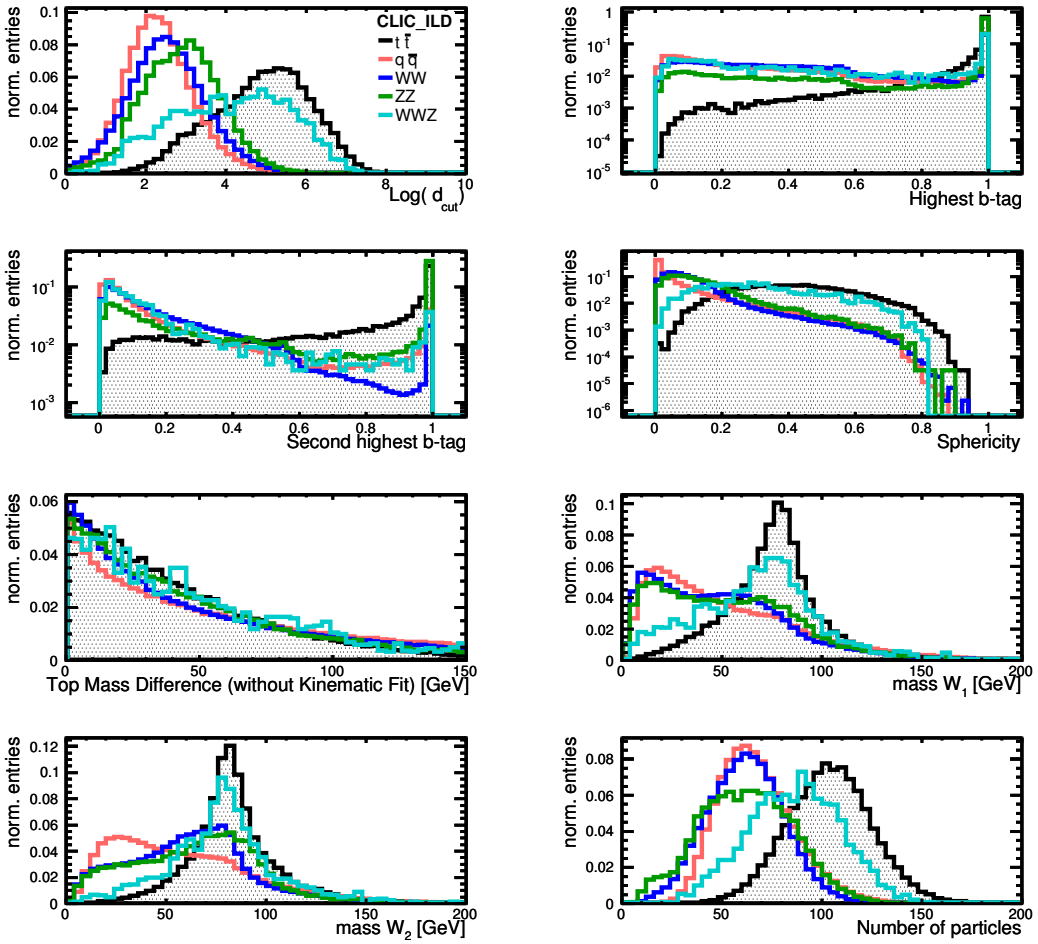

Figure 8: Distribution of the input variables of the background rejection. The black lines represent the signal, the other colored lines represent the background. All distributions are normalized to the same integral.

	Signal efficiency [%]	Background rejection efficiency [%]
4 jet channel	93.5	98.0
6-jet channel	94.4	96.7

Table 4: Signal and background rejection efficiency of the likelihood technique for the event sample passing the kinematic fit.

4.7. Top Mass and Width Measurement

The top mass and width are extracted using an unbinned likelihood fit of the final top mass distribution of events (signal and background) after kinematic fit and background rejection. The

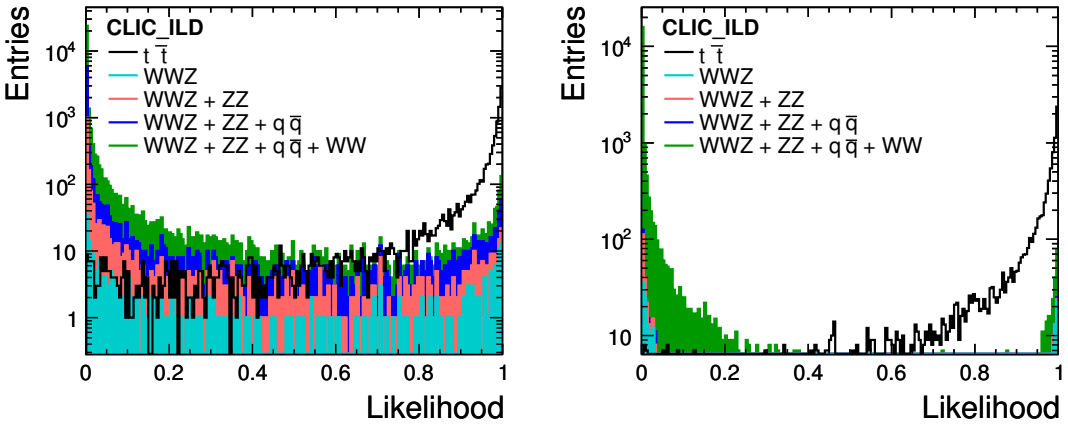

Figure 9: Likelihood for physics processes to belong to the signal events class for 6-jet events (*left*) and 4 jet events (*right*). A cut at a likelihood value of 0.6 was chosen to reject background events for the 6-jet and 4 jet event sample. The different background processes are stacked on top of each other. The signal is not stacked.

fit function consists of three components, which account for physics background, the detector resolution and the signal itself. The first two are determined in constrained fits prior to the fit of the final distribution, resulting in a three step approach to the mass fit:

1. Fit of the true background events only to determine a background parametrization.
2. Fit of the true signal events only to determine the detector resolution function on an independent event sample with approximately twice the statistics (see Table:1).
3. Final fit of measured top mass distribution with true signal and background events classified by the background rejections as events belonging to the signal class.

To parametrize the background, a threshold function was used, in which the threshold was fixed to $a = 100\,\text{GeV}$.

$$\text{bkg\_pdf} = (x-a)^b$$

For the bkg_pdf fit the parameter b was left free. The final parameters for the fitted background distribution can be found in Appendix A.5.
For the signal fit, the following PDF was used:

$$\begin{aligned}\text{sig\_pdf} &= f \cdot \text{BreitWigner}(m_{\text{bw}}, \sigma_{\text{bw}}) \otimes (\text{Gauss1} + \text{Gauss2} + \text{Gauss3}) \\ &\quad + (1-f) \cdot \text{GaussTail}\end{aligned}$$

This fit consists of two main components, a signal part described by a Breit-Wigner convolved with a detector resolution function implemented by the sum of three Gaussians, and a background part labeled *GaussTail* to account for the high-mass tail observed in the signal at masses

around 230 GeV. This tail is due to kinematic reflections in events with incorrect assignments of jets and/or leptons to top candidates. The mean value of the Breit-Wigner is given by m_{bw}, and the corresponding width by σ_{bw}. The relative fraction of the two components is described by the the factor f.

The detector resolution component of the signal part is described by

$$\begin{aligned} \text{Gauss1 + Gauss2 + Gauss3} \quad = \quad & (f1 \cdot \text{Gauss1}(x, m1, s1)) + \\ & (f2 \cdot \text{Gauss2}(x, m2, s2)) + \\ & ((1.0 - f1 - f2) \cdot \text{Gauss3}(x, m3, s3)), \end{aligned}$$

where the notation Gauss(x, mean, sigma) is used and $f1$ and $f2$ are the fractions of the Gaussians in the sum. This function does not only represent the detector resolution, but also accounts for systematic effects introduced by the analysis chain and by the pick-up of $\gamma\gamma \rightarrow$ hadrons background.

For the fit of the true signal distribution to determine the resolution function a statistically independent event sample was used. The mean and width for the Breit-Wigner component were fixed to the generator values of $m_{\mathrm{bw}} = 174.0\,\mathrm{GeV}$ and $\sigma_{\mathrm{bw}} = 1.37\,\mathrm{GeV}$. All parameters of the Gaussian sum were left free. The resulting final parameters of the fit are listed in Appendix A.5. To exclude a bias from using the same input values as for the data sample, the parameter adjustment was also performed on a sample with a mass of 175 GeV and a width of 1.5 GeV, as discussed below.

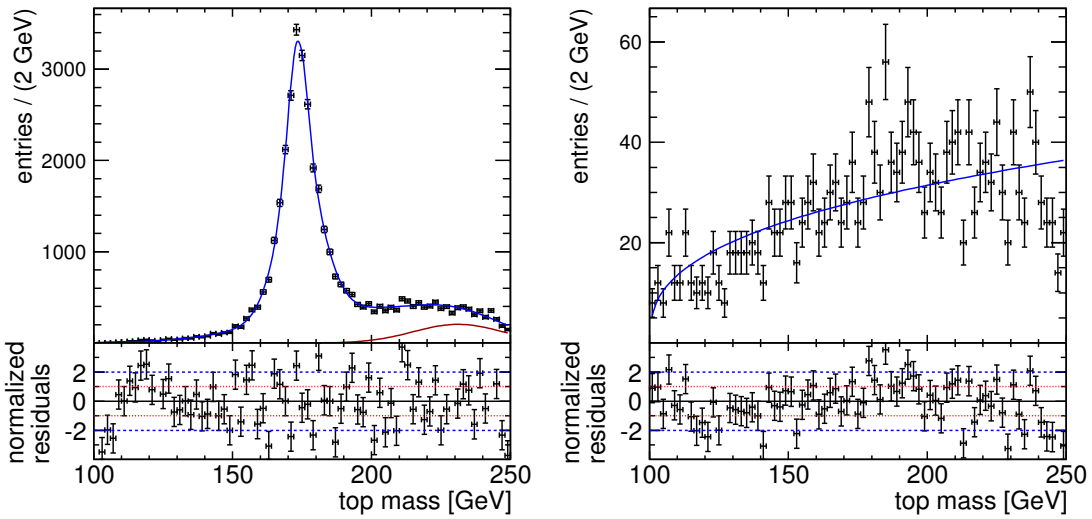

Figure 10: Pure signal distribution (*left*) and pure background distribution (*right*) for the 6-jet events. Black points with error bars show the simulated data, while the blue line indicates the signal fit of the sig_pdf. The red line indicates the fit of the GaussTail, which is part of the signal fit.

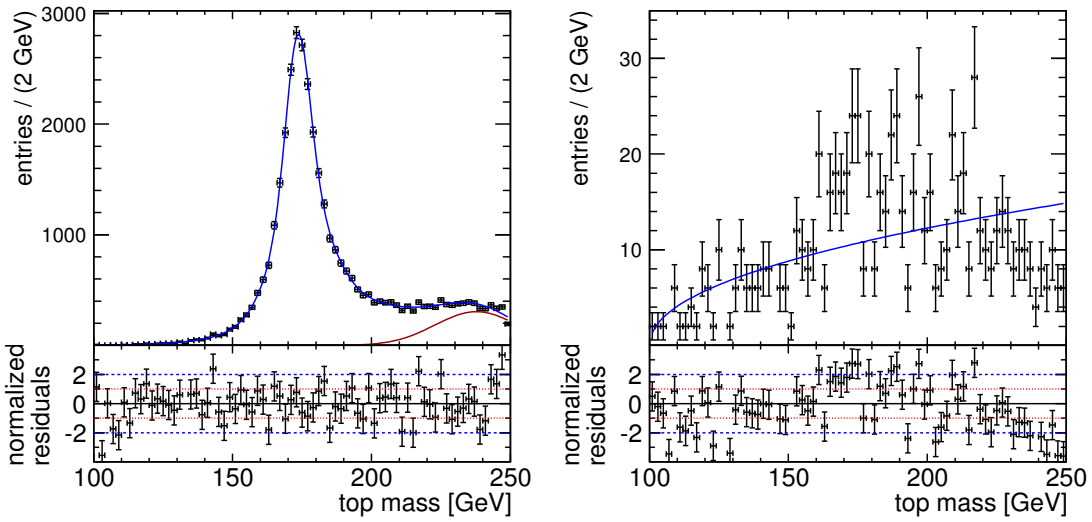

Figure 11: Pure signal distribution (*left*) and pure background distribution (*right*) for the 4 jet events. Black points with error bars show the simulated data, while the blue line indicates the signal fit of the sig_pdf. The red line indicates the fit of the GaussTail, which is part of the signal fit.

Figures 10 and 11 show the fits to the signal only and background only distributions for the fully-hadronic and the semi-leptonic event samples, respectively.

The final fit function for the top mass distribution containing signal and background is given by the sum of the signal and background functions,

$$\text{pdf} = y_{\text{Signal}} \cdot \text{sig\_pdf} + y_{\text{Background}} \cdot \text{bkg\_pdf},$$

where y_{Signal} and $y_{\text{Background}}$ describe the signal and background yield, respectively. In the final fit, fixed values for the Gaussians of pdf_bkg and pdf_sig were used, leaving only $m_{\text{bw}}, \sigma_{\text{bw}}$, y_{Signal} and $y_{\text{Background}}$ as free parameters.

The fit was performed independently for the fully-hadronic and for the semi-leptonic events. The fit of the overall distribution is shown by the line in Figure 12.

The resulting top mass is

$$m_{\text{top}} = 174.07\,\text{GeV} \pm 0.08\,\text{GeV}$$

for the all-hadronic sample, and

$$m_{\text{top}} = 174.28\,\text{GeV} \pm 0.09\,\text{GeV}$$

for the semi-leptonic sample. The generated top mass was 174 GeV, thus the all-hadronic mass is in excellent agreement with the input value, while the semi-leptonic measurement differs by three standard deviations. This deviation is likely mostly due to uncertainties of the detector

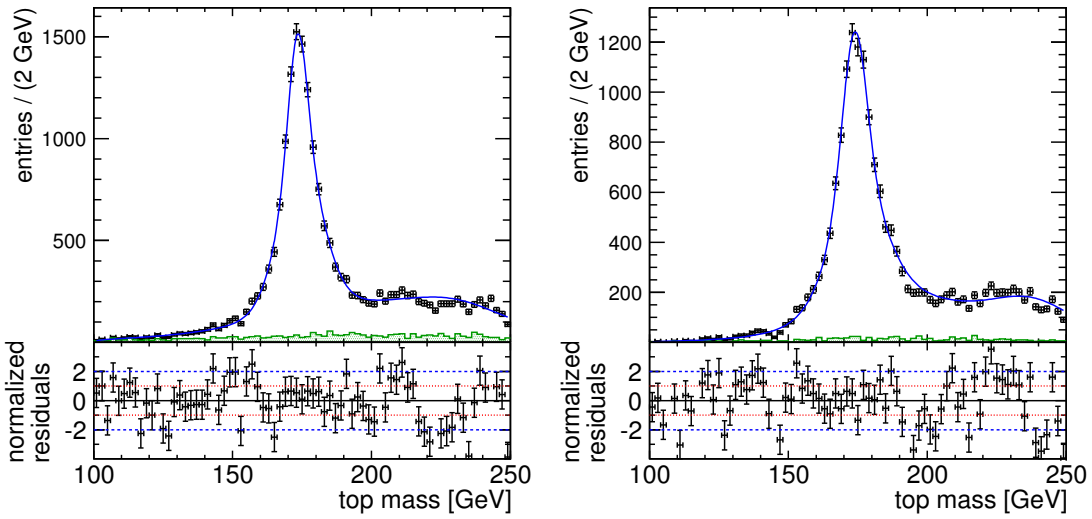

Figure 12: Final top mass distribution for 6-jet events (*left*) and 4 jet events (*right*). Black points with error bars show simulated data classified as signal events. The green hatched histogram represents the physics background. The blue line indicates the fit of the top mass distribution.

resolution function, which was determined from a statistically independent sample of approximately two times the integrated luminosity compared to the signal sample.

The test of the fit with another fit training sample with a mass of 175 GeV and a width of 1.50 GeV, discussed further in Appendix A.7, has led to results consistent with the ones presented here. This shows that no significant bias resulting from the generator mass for the fit training sample exists. Consistent results were also obtained with a different fit function, as used in the ILD LoI [7], as discussed in Appendix A.6.

The determination of the top width is more challenging, and depends strongly on the used data sample for the fit adjustment and on the choice of the fit function, in particular in the semi-leptonic case. For the all-hadronic sample, a width of

$$\sigma_{\text{top}} = 1.33\,\text{GeV} \pm 0.21\,\text{GeV}$$

was obtained, to be compared with a generator level value of 1.37 GeV. For the semi-leptonic sample, a width of

$$\sigma_{\text{top}} = 1.55\,\text{GeV} \pm 0.26\,\text{GeV}$$

was found, also in good agreement with the generator value.

This study shows that the top mass can be determined at a 500 GeV CLIC with comparable statistical precision to the resolutions obtained for ILC in the ILD LoI in both the fully-hadronic and semi-leptonic decay channels, despite the more challenging experimental environment at CLIC. A comparison of the reconstructed top mass distributions obtained with the present analysis and with the ILD detector concept at ILC is presented in Appendix A.6.

4.8. Cut Flow Table

The overall signal reconstruction efficiency, combining kinematic fit success rate and rejection with the likelihood technique achieved in the present analysis is comparable to the ILD LoI analysis in the fully-hadronic channel, and even exceeds it in the semi-leptonic channel. The numbers of accepted events in the different analysis branches at various steps in the analysis are summarized in Table 5. The overall selection efficiency for true fully-hadronic top pair decays in the 6 jet branch was 35%, and the overall efficiency for true semi-leptonic top pair decays in the 4 jet branch was 56%.

$gg \to$ hadron events overlaid

	Signal		Background	
Analysis step	6 jet sample	4 jet sample	6 jet sample	4 jet sample
	52780		1014000	
LeptonFinder	30973 (23305 true)	18617 (13619 true)	733421	241672
Kinematic Fit	8701	8230	30718	19776
Background Rejection	8217	7691	1018	400

Table 5: Summary of the cut flow of the analysis.

5. Conclusions

The mass of the top quark is one of the key parameters of the standard model, and provides sensitivity to new physics. The present study, using full simulations including machine and physics backgrounds, carried out in the framework of the CLIC CDR, has shown that a 500 GeV linear e^+e^- collider based on CLIC technology is an excellent tool for precision top measurements. $\gamma\gamma \to$ hadrons background can be controlled by the event reconstruction, and has only small effects on the flavor tagging. Precise reconstruction of the event kinematics is achieved by means of a kinematic fit, which also serves to control the energy uncertainty due to the beam energy spectrum and contributes to the rejection of non-$t\bar{t}$ background. With an integrated luminosity of 100 fb^{-1}, a statistical precision of 80 MeV was achieved in the fully-hadronic decay channel, and a precision of 90 MeV was achieved in the semi-leptonic channel. This precision is comparable to that expected for the ILC, despite the more challenging experimental environment at CLIC.

References

[1] Tevatron Electroweak Working Group, and the CDF and D0 Collaborations. Combination of CDF and DO results on the mass of the top quark using up to 5.8 fb-1 of data. *arXiv:1107.5225*, 2011.

[2] The ATLAS Collaboration. Measurement of the top-quark mass from 2011 atlas data using the template method. *ATLAS-CONF-2011-120*, 2011.

[3] The CMS Collaboration. Measurement of the top quark mass in the l+jets channel. *CMS PAS TOP-10-009*, 2011.

[4] G. Aad et al. Expected Performance of the ATLAS Experiment - Detector, Trigger and Physics. *arXiv:0901.0512*, 2009.

[5] S. Fleming, A. H. Hoang, S. Mantry, and I. W. Stewart. Jets from massive unstable particles: Top-mass determination. *Phys.Rev.*, vol. D77 p. 074010, 2008.

[6] S. Fleming, A. H. Hoang, S. Mantry, and I. W. Stewart. Top Jets in the Peak Region: Factorization Analysis with NLL Resummation. *Phys.Rev.*, vol. D77 p. 114003, 2008.

[7] The ILD Concept Group. International Large Detector - Letter of Intent. *DESY 2009/87, Fermilab PUB-09-682-E, KEK Report 2009-6LCD-Note-2011-002*, 2010.

[8] A. Münnich and A. Sailer. The CLIC ILD CDR Geometry for the CDR Monte Carlo Mass Production. *LCD-Note-2011-002*, 2011.

[9] WHIZARD. Website: `http://projects.hepforge.org/whizard/`.

[10] PYTHIA. Website: `http://home.thep.lu.se/~torbjorn/Pythia.html`.

[11] A. S. D. Dannheim. Beam-Induced Backgrounds in the CLIC Detectors. 2011.

[12] O. S. T. Barklow, D. Dannheim and D. Schulte. Simulation of $\gamma\gamma \to$ hadrons background at CLIC. 2011.

[13] Mokka. Website: `http://polzope.in2p3.fr:8081/MOKKA/`.

[14] M. Cacciari and G. Salam. Dispelling the N3 myth for the Kt jet-finder. *Phys. Lett.*, 2006. B641 [hep-ph/0512210].

[15] LCFI Vertex Package. Website: `http://www-pnp.physics.ox.ac.uk/~hillert/VP/LCFIVertex-v00-01/`.

[16] MarlinKinFit. Website: `http://ilcsoft.desy.de/MarlinReco/current/doc/html/kinfit.html`.

[17] J. Marshall, A. Münnich, and M. A. Thomson. PFA: Particle Flow Performance at CLIC. *LCD-Note-2011-028*, 2011.

[18] The OPAL collaboration. Search of the Standard Model Higgs Boson in e^+e^- collisions at $\sqrt{s} = 161$ - 172GeV. *Eur.Phys.Jour.*, 1998. C 1, 425.

[19] R. Hawkings. Vertex detector and flovour tagging studies for the tesla linear collider, 2000. LC-PHSM-2000-021-TESLA.

A. Appendix

A.1. Default CLIC selector cuts for 500GeV

Region	p_t *range*	Time cut
Photons		
central	1.0 GeV $\leq p_t <$ 2.0 GeV	$t <$ 5.0 nsec
($\cos\theta \leq 0.975$)	0 GeV $\leq p_t <$ 1.0 GeV	$t <$ 2.5 nsec
forward	0.75 GeV $\leq p_t <$ 4.0 GeV	$t <$ 2.0 nsec
($\cos\theta > 0.975$)	0 GeV $\leq p_t <$ 0.75 GeV	$t <$ 1.0 nsec
Neutral hadrons		
central	1.0 GeV $\leq p_t <$ 2.0 GeV	$t <$ 5.0 nsec
($\cos\theta \leq 0.975$)	0 GeV $\leq p_t <$ 1.0 GeV	$t <$ 2.5 nsec
forward	2.0 GeV $\leq p_t <$ 4.0 GeV	$t <$ 2.0 nsec
($\cos\theta > 0.975$)	0 GeV $\leq p_t <$ 2.0 GeV	$t <$ 1.0 nsec
Charged PFOs		
all	1.0 GeV $\leq p_t <$ 4.0 GeV	$t <$ 10.0 nsec
	0 GeV $\leq p_t <$ 1.0 GeV	$t <$ 3.0 nsec

A.2. Flavor Tagging Input Variables

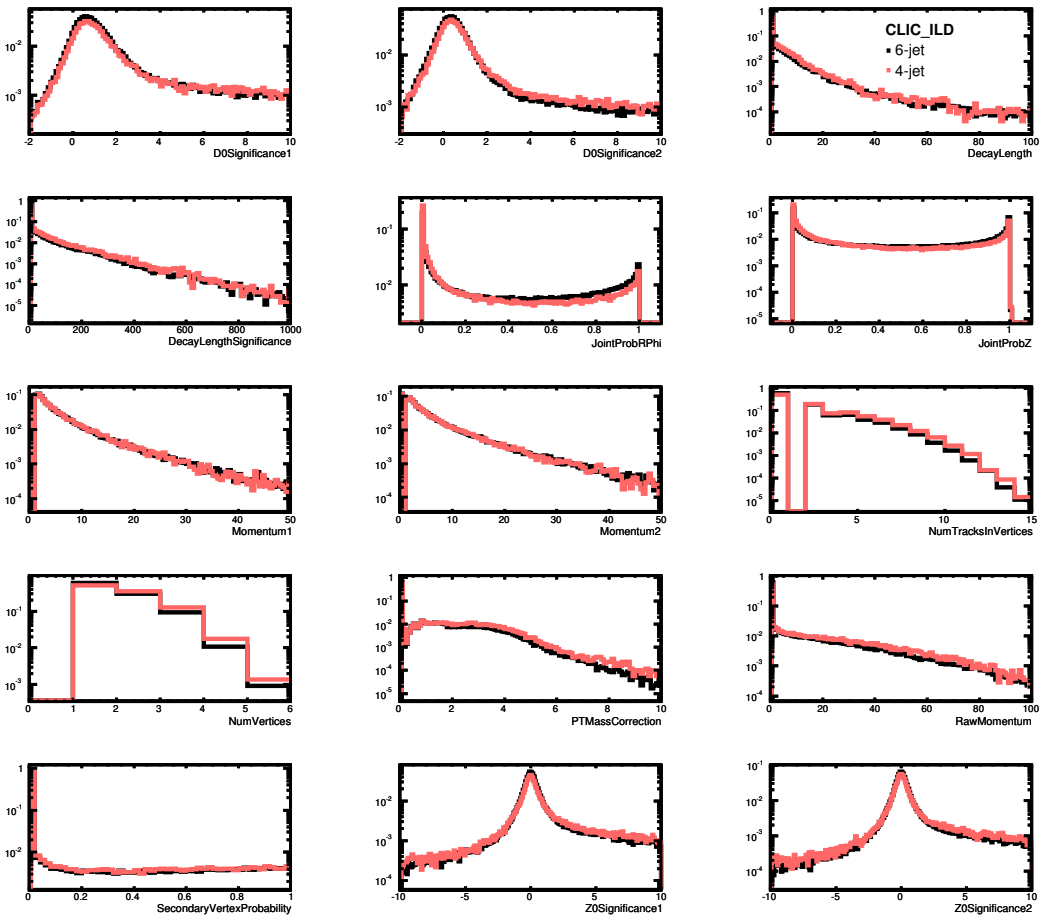

Figure 13: Input variables of the flavor tagging algorithms. Shown are the input variables distributions for the signal event in the 6 and 4 jet event samples. A detailed description of the variables can be found in [15, 19].

A.3. Lepton and Jet angle and energy resolution

The energy and angular resolutions of leptons and jets were studied by comparing the reconstructed objects to the generator level values. In the case of jets, the comparison was made with respect to quarks. Here, a jet was associated to one specific quark if it was closest to that particular jet, and it was required that this procedure led to unique assignments of all jets and leptons in the event to generator-level particles. This unique assignment was successful for 58 % of all fully-hadronic events and for 65% of all semi-leptonic events. These numbers can also be taken as an indication of the success of the jet clustering, and put the failure rates of the kinematic fit (often due to reconstruction issues) into perspective.

The angular resolution of the leptons and jets, as well as the energy resolution of the leptons (averaged for electrons and muons for simplicity) were used as parameters for the kinematic fit. The significant overlap between jets in the dense multi-jet environment of $t\bar{t}$ events results in a degradation of the single jet energy resolution. However, since the mis-reconstruction of the jets in the event are correlated, this resolution does not correctly reflect the effect on the invariant mass resolution, and thus can not be used as parameter in the kinematic fit. Instead, the single jet resolution for di-jet events was used.

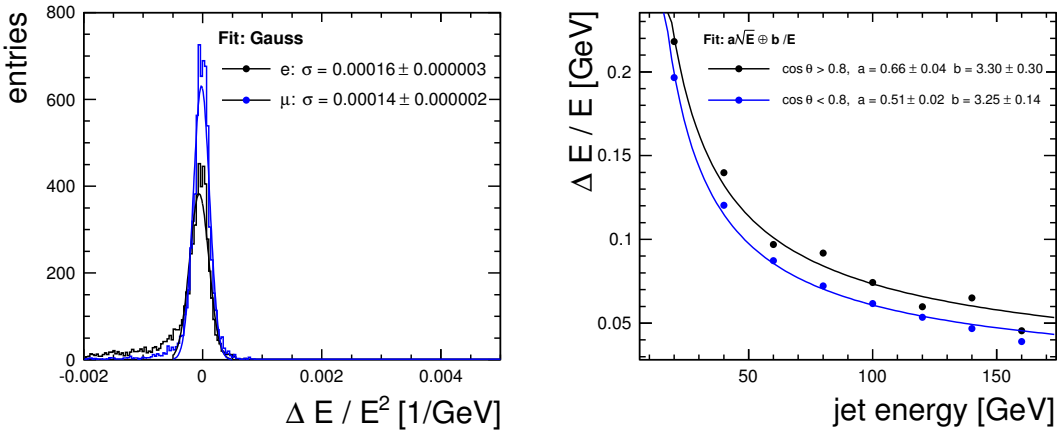

Figure 14: Energy resolution of leptons (*left*) and jets (*right*).

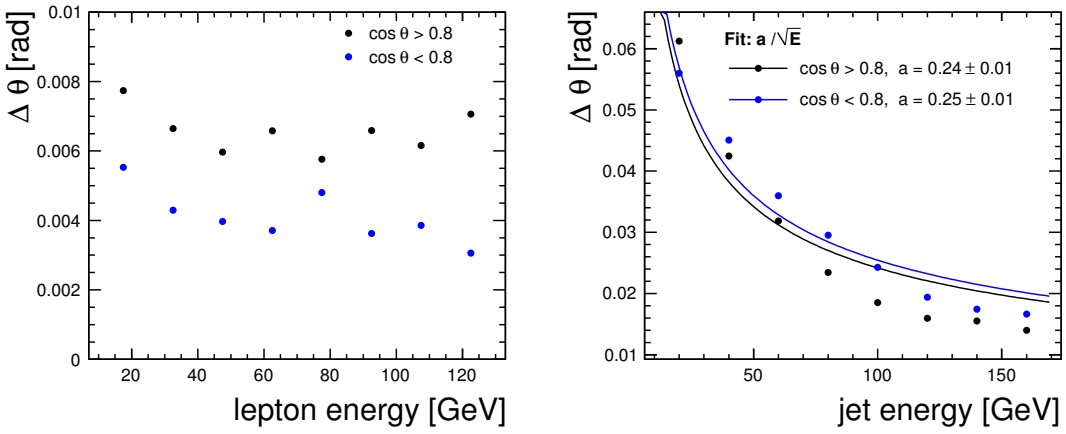

Figure 15: Angular resolution of θ for leptons (*left*) and jets (*right*).

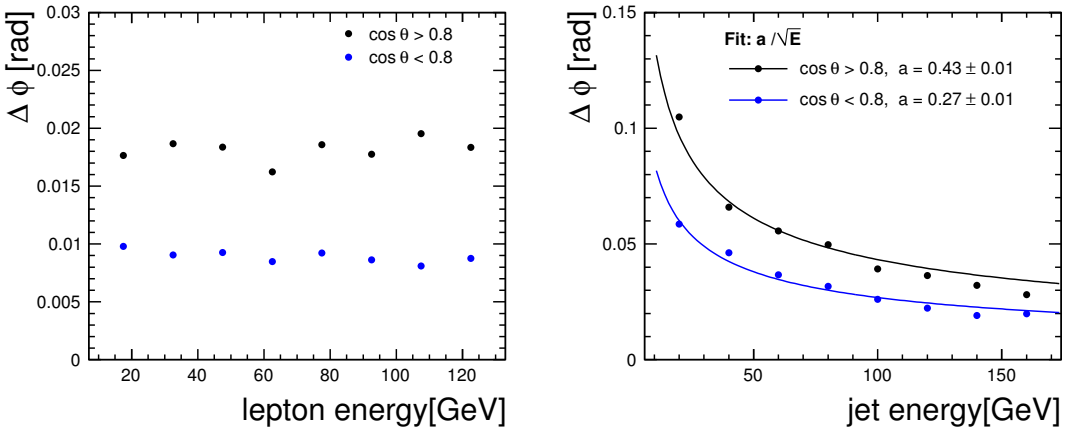

Figure 16: Angular resolution of ϕ for leptons (*left*) and jets (*right*).

A.4. Kinematic fit - successful and unsuccessful

The reasons for the failure of the kinematic fit have been investigated by studying the reconstructed invariant mass without kinematic fit for events that pass or fail the fit. This shows quite clearly that mis-reconstructed W bosons are responsible for a significant fraction of the failed kinematic fits (see Figures 17 and 18).

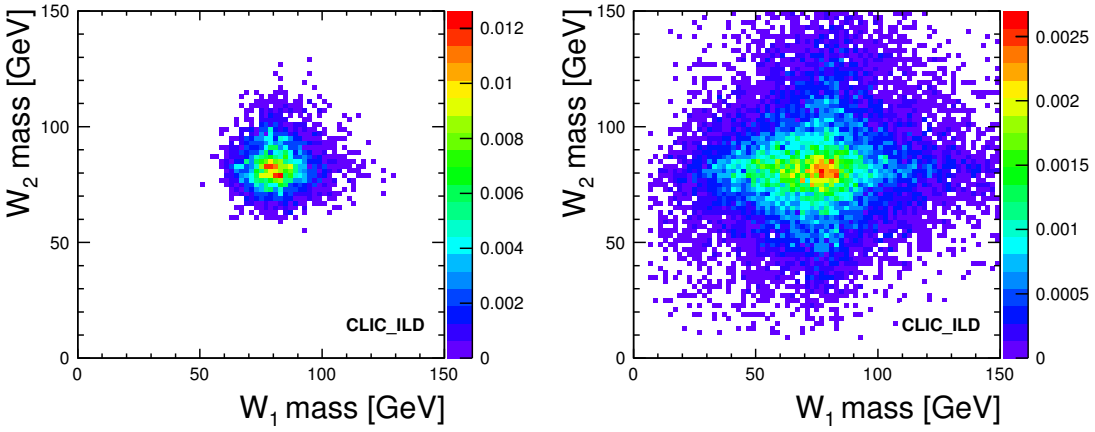

Figure 17: Reconstructed masses of the W bosons before the kinematic fit for the 6-jet event sample of the signal events. *Left:* successful kinematic fit. *Right:* Unsuccessful kinematic fit. Events with reconstructed W bosons masses far from 80.4 GeV do not lead to a successful kinematic fit.

Another important factor for the failure of the kinematic fit was the center of mass energy of the event, which can deviate substantially from 500 GeV for events with large beamstrahlung. In particular in the fully-hadronic event sample, this results in failures of the kinematic fit. In the semi-leptonic case, also events with large beamstrahlung can pass the fit, which is partially responsible for the increased width of the invariant mass distribution.

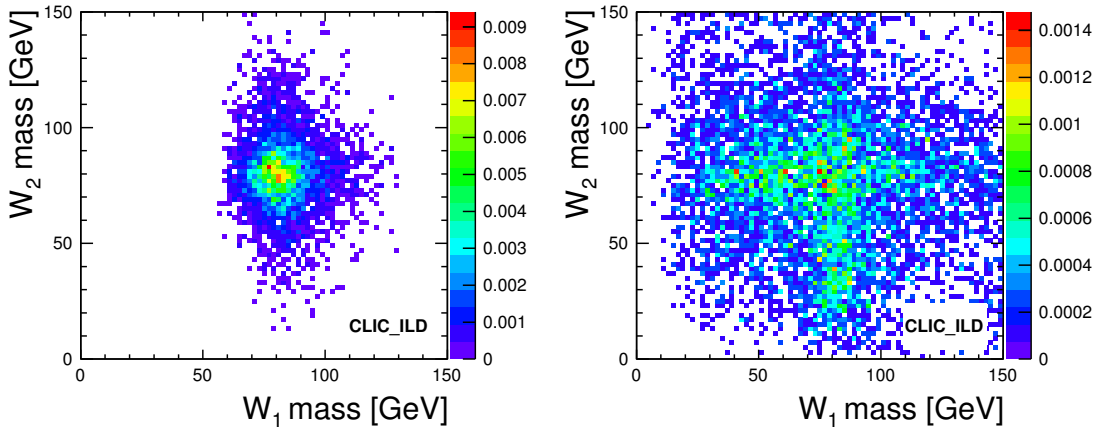

Figure 18: Reconstructed masses of the W bosons before the kinematic fit for the 4 jet event sample of the signal events. *Left:* successful kinematic fit. *Right:* Unsuccessful kinematic fit. Events with reconstructed W bosons masses far from 80.4 GeV do not lead to a successful kinematic fit.

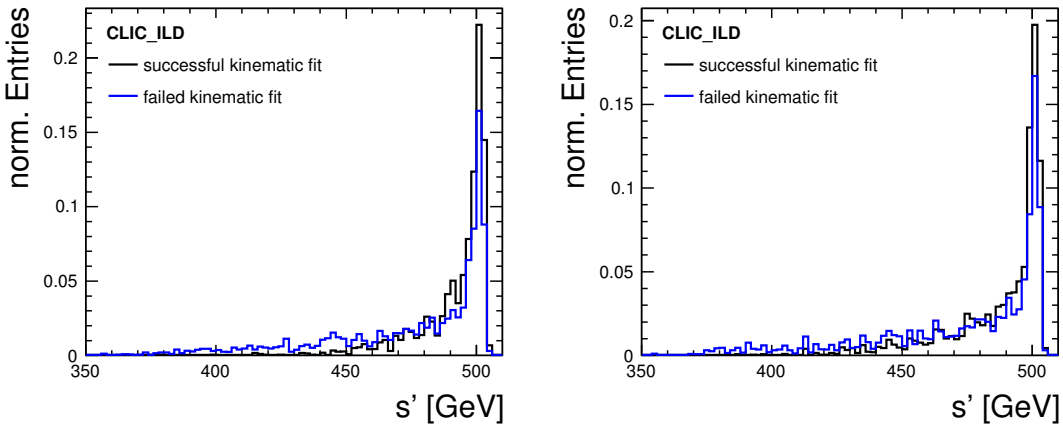

Figure 19: s' on generator level of the signal events for the 6-jet event sample (*left*) and the 4 jet event sampple (*right*). The relation between an unsuccessful kinematic fit and large beamstrahlung is more evident for 6-jet events. In the 4 jet event sample the kinematic kit can recover the energy loss due to the neutrino (MarlinKinFit: NeutrinoFitObject).

A.5. PDF parameters

A complete list of the parameters of the final mass fit.
Background pdf:

- $p_0 = 100$, fixed
- $p_1 = 0.37 \pm 0.03$

for the 6-jet event sample and

- $p_0 = 100$, fixed
- $p_1 = 0.48 \pm 0.05$

for the 4 jet event sample.

Signal pdf:

- $m_1 = -0.61 \pm 0.10$, $s_1 = 3.11 \pm 0.26$
- $m_2 = 1.19 \pm 0.23$, $s_2 = 2.44 \pm 0.11$
- $m_3 = 21.45 \pm 3.46$, $s_3 = 4.01 \pm 0.28$
- $f_1 = 0.20 \pm 0.04$, $f_2 = 0.43 \pm 0.03$
- $m_{tail} = 231.14 \pm 1.60$, $s_{tail} = 16.00 \pm 2.06$

for the 6-jet event sample and

- $m_1 = -0.47 \pm 0.11$, $s_1 = 4.04 \pm 0.20$
- $m_2 = 1.46 \pm 0.29$, $s_2 = 2.36 \pm 0.10$
- $m_3 = 16.06 \pm 3.28$, $s_3 = 2.60 \pm 0.14$
- $f_1 = 0.28 \pm 0.03$, $f_2 = 0.36 \pm 0.02$
- $m_{tail} = 237.74 \pm 1.03$, $s_{tail} = 14.84 \pm 1.18$

for the 4 jet event sample.

A.6. Comparison with ILD LoI results

For the comparison of the $t\bar{t}$ analysis at CLIC with the one at ILC the results presented in the ILD Letter of Intent (LoI) [7] were used and directly compared with the results presented in this note as shown in Figure 20. Both studies correspond to an integrated luminosity of $100\,\mathrm{fb}^{-1}$. The distributions show that in the case of fully-hadronic top events ($t\bar{t} \to bq\bar{q}\bar{b}q\bar{q}$), the CLIC_CDR results gives a slightly narrower and higher peak of the top quark mass with similar statistics, showing comparable overall efficiency. Also the non-$t\bar{t}$ background is lower in the present analysis. For the semi-leptonic decay channel ($t\bar{t} \to bq\bar{q}bl\nu_l$) the peak is nearly twice as high, but also broader than the ILD LoI top mass peak. The physics background is comparable. The most likely reason for this difference is the introduction of a neutrino fit object in MarlinKinFit as explained Section 4.5, which results in a higher success rate of the fit and the more difficult beam background and beam energy conditions at CLIC, which result in increased uncertainty of the neutrino energy.

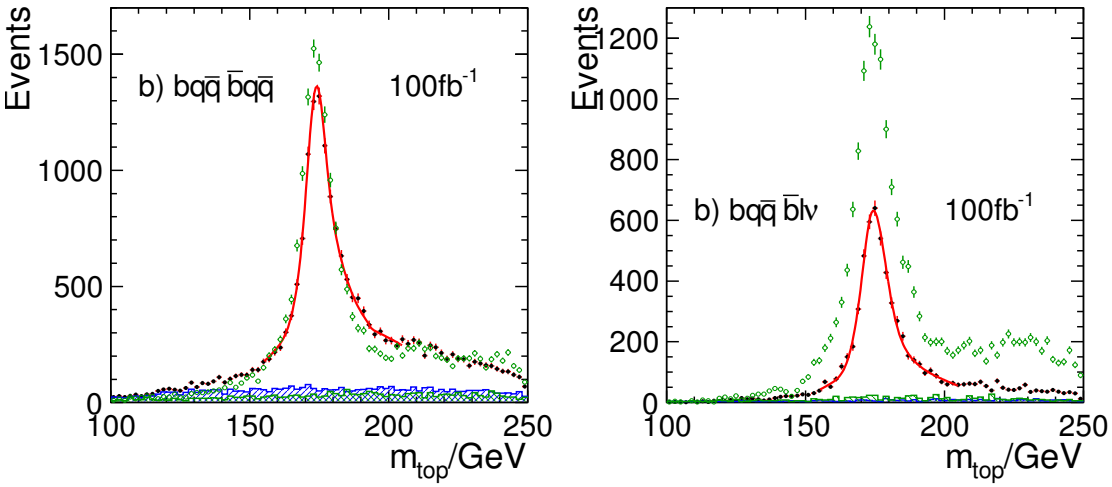

Figure 20: Comparison with the results of the ILD LoI, showing the results of the present study on top of the corresponding plot taken from the ILD LOI.
The black points show the top mass distribution obtained for the $t\bar{t}$ analysis of the ILD LoI. The blue histogram shows the physics background of the distribution and the red line represents the final fit. The green points and the green histogram show the top mass distribution and the physics background respectively for the CLIC CDR analysis.

To study if the final fit is the only reason for the difference between generator top mass and width and the final CLIC results, the fit used in the ILD LoI was tested as well. The ILD LoI fit is a binned χ^2 fit of tree steps:

1. Fit of physical background events only with a polynomial of order 2.

2. Fit of signal events only with a convolution of a Breit-Wigner and a detector resolution function. For the detector resolution function a asymmetric double Gaussian was chosen. The parameters of the Breit-Wigner were fixed to the generator values of top mass and with of the used sample. For the LoI a high statistics sample corresponding to an integrated luminosity of $2.8\,\mathrm{ab}^{-1}$ was used. For this study a statistically independent signal sample corresponding to $200\,\mathrm{fb}^{-1}$ was used.

3. The third step was the fit of the final top mass distribution with a combination of signal and background fit. In the final fit all parameters defining the shapes of the combinatoric background, physical background and detector resolution function, have been fixed to the fit results of the first two steps. The only free parameters in this fit were therefore the top mass, width and the overall normalization.

The results are shown in Figure 21 for the fully-hadronic (left) and semi-leptonic (right) decay channels, respectively. Here, the training samples of signal only events were generated with a top mass of 174.0 GeV and a top width of 1.37 GeV. In Figure 22 the results are shown for the full-hadronic (left) and semi-leptonic (right) channel using a training sample with a generated top mass of 175.0 GeV and a width of 1.5 GeV. The obtained values using the LoI fit for the top mass determination are generally 0.5 % lower than for the fit described in Subsection 4.7 and thus are not compatible with a generated top mass of 174 GeV, which is used in the final signal sample. The size of the statistical error on the top mass is approximately the same in both cases. The fact that nearly the same values for the top mass are obtained independent of the generated top mass used in the events for the signal only fit (trainings sample), indicates that no significant bias from the training samples exists. Compared to the values obtained with the unbinned maximum likelihood fit used to obtain the results for the present study, the LoI fit gives a significantly smaller fit error for the top quark width. Considering the discrepancy of the generator value and the measured value, the size of this error seems to be underestimated. Due to its construction, the LoI fit exhibits stability issues and shows a high sensitivity to the fit range, which is avoided by a fit over the full range in the CLIC study.

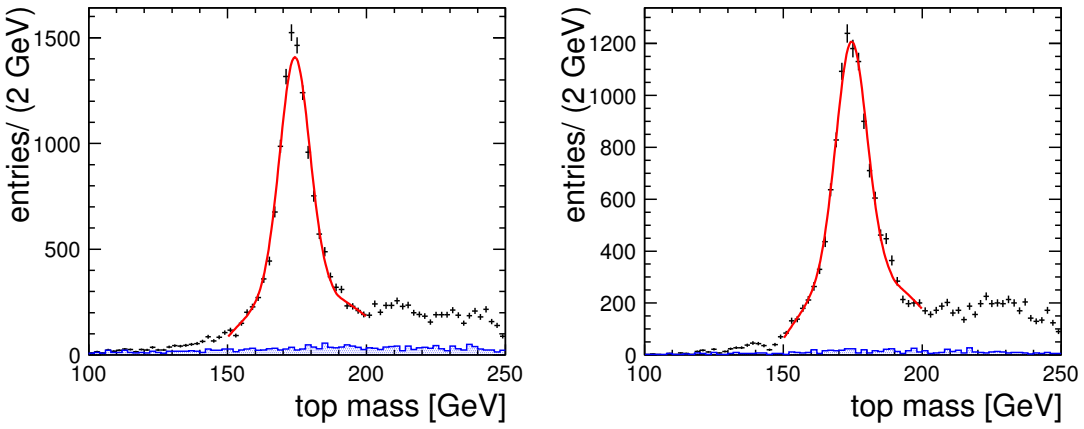

Figure 21: CLIC top mass distribution (black points) and physics background distribution (blue histogram) with top mass peak fit (red line) obtained with the same fit function used in the ILD LoI. The signal only fit of step two was done with an event sample of generator top mass of 174.0 GeV and width of 1.37 GeV.
Results for the full-hadronic event sample (*left*): $m_{top} = 173.18\,\text{GeV} \pm 0.10\,\text{GeV}, \sigma_{top} = 1.56\,\text{GeV} \pm 0.07\,\text{GeV}$.
Results for the semi-leptonic event sample (*right*): $m_{top} = 173.50\,\text{GeV} \pm 0.08\,\text{GeV}, \sigma_{top} = 1.65\,\text{GeV} \pm 0.08\,\text{GeV}$.

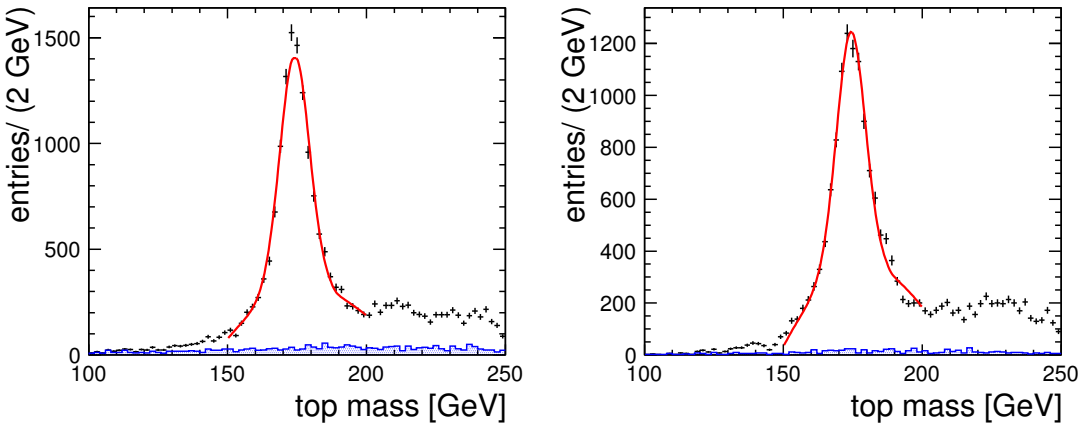

Figure 22: Top mass distribution (black points) and physics background distribution (blue histogram) with top mass peak fit (red line) obtained with the same fit function used in the ILD LoI. The signal only fit of step two was done with an event sample of generator top mass of 175.0 GeV and width of 1.5 GeV.
Results for the full-hadronic event sample (*left*): $m_{top} = 173.15\,\text{GeV} \pm 0.08\,\text{GeV}, \sigma_{top} = 1.73\,\text{GeV} \pm 0.08\,\text{GeV}$.
Results for the semi-leptonic event sample (*right*): $m_{top} = 173.33\,\text{GeV} \pm 0.11\,\text{GeV}, \sigma_{top} = 1.55\,\text{GeV} \pm 0.07\,\text{GeV}$.

A.7. Test of the final fit using different event samples

To test the stability of the fit, and to confirm the origin of the observed shift from the true mass, two tests were carried out: Training the fit with a sample with a higher mass, and exchanging training and data sample. In the former case, consistent results with the final fit in the note were obtained, suggesting that no bias from the mass of the training sample exists. In the latter case, opposite shifts in mass were observed as expected. showing reproducible and stable performance of the fit.

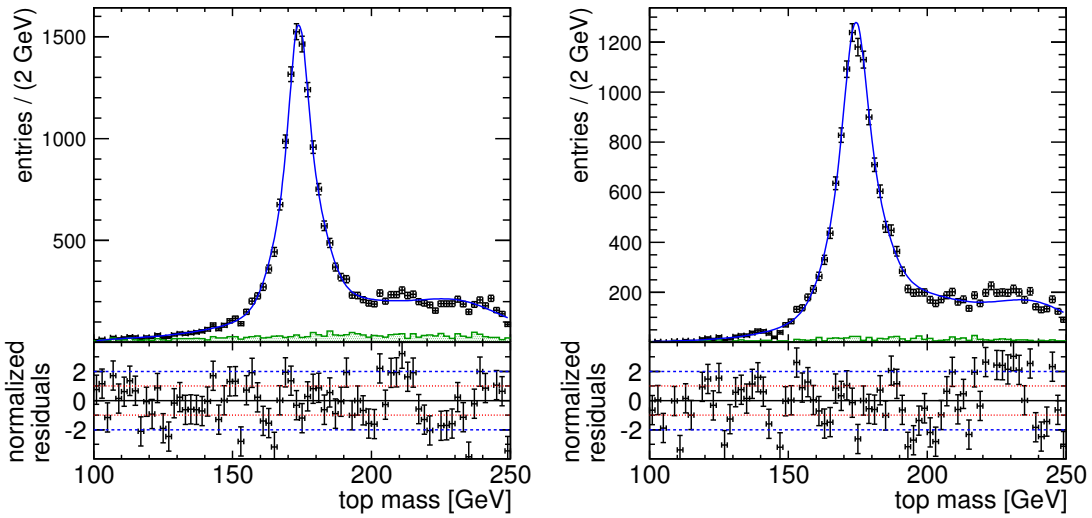

Figure 23: Final top mass distribution fitted with pdf described in 4.7. For the fit training sample a sample was used with a generated top mass of 175.0 GeV and width of 1.5 GeV.
Results for the final full-hadronic sample: $m_{top} = 173.96\,\text{GeV} \pm 0.07\,\text{GeV}, \sigma_{top} = 0.66\,\text{GeV} \pm 0.23\,\text{GeV}$.
Results for the final semi-leptonic sample: $m_{top} = 174.28\,\text{GeV} \pm 0.09\,\text{GeV}, \sigma_{top} = 1.77\,\text{GeV} \pm 0.25\,\text{GeV}$